Available online at www.sciencedirect.com
SCIENCE DIRECT
Journal of Magnetic Resonance 179 (2006) 73–84
JMR Journal of Magnetic Resonance
www.elsevier.com/locate/jmr

Dynamics of ^{23}Na during completely balanced steady-state free precession

Reza Kharrazian *, Peter M. Jakob

Department of Experimental Physics 5, University of Würzburg, Würzburg, Germany

Received 26 September 2005; revised 7 November 2005
Available online 6 December 2005

Abstract

The dynamics of ^{23}Na during completely balanced steady-state free precession (SSFP) have been studied in numerical simulations and experiments. Results from both agree well. It is shown that during SSFP multiple quantum coherences are excited and that their excitation affects the observable signal. The signal response to the sequence parameters (flip angle, TR, and RF pulse phase cycle) shows a structure which can not be described by the Bloch equations. Due to excitation of $\hat{T}_{31}(s,a)$, the amplitude ratio of the fast and slowly decaying components deviates from 3:2 and is a function of the sequence parameters. The results shown here represent a basis for the implementation and optimization of ^{23}Na-SSFP imaging sequences.

Keywords: ^{23}Na; Steady-state free precession; Quadrupolar relaxation; Sodium

1. Introduction

Steady-state free-precession (SSFP) methods [1] have found widespread application in ^{1}H magnetic resonance imaging due to their high signal-to-noise ratio (SNR) and interesting contrast properties [2]. Since the first report of SSFP imaging in 1986 [3], improvements in scanner hardware, in particular, gradient stability, better shim algorithms and better RF phase stability, have resolved most of the initial shortcomings. An important question to be considered is whether the advantages of SSFP methods can be used for imaging and spectroscopy with X-nuclei as well. The use of SSFP chemical shift imaging with ^{31}P has been demonstrated [4]. Another X-nucleus to be considered is ^{23}Na.

^{23}Na plays an important role in applications of biology, chemistry, and medicine. For instance, sodium has been proposed as a means to measure tissue viability and to detect myocardial infarction [5–8]. In this context, a TrueFISP sequence has been previously used to obtain ^{23}Na MR images of the heart [5]. Other important applications are the characterization of cartilage [9], imaging of the kidney [10], and brain [11], and the study of polymers in the liquid state [12].

The mathematical framework for the description of the magnetization vector with spin-1/2 nuclei is the Bloch equations. Based on these, the dynamics of ^{1}H, ^{31}P, and other spin-1/2 nuclei during SSFP are well understood [1,2,13]. However, an analogous understanding is missing for ^{23}Na (and spin-3/2 nuclei in general). ^{23}Na is a nucleus with a quadrupolar moment which dominates its relaxation characteristics. Quadrupolar relaxation causes the excitation of multiple quantum coherences and biexponential decay; these are effects which can not be described by the Bloch equations. It is therefore obvious that with ^{23}Na, the SSFP dynamics are fundamentally different than with spin-1/2 nuclei. The question addressed in this paper is, however, whether the differences in the underlying dynamics also lead to distinct differences in the observable signal. Since this is closely related to the excitation of coherences of rank $l > 1$, the question addressed is to what extent these coherences are excited and how this depends on the sequence parameters (TR, flip angle, and RF pulse phase cycle). To the best of our knowledge, this issue has not been

* Corresponding author. Fax: +49 (0) 931 888 5851.
E-mail address: rakharra@physik.uni-wuerzburg.de (R. Kharrazian).

1090-7807/$ - see front matter © 2005 Elsevier Inc. All rights reserved.
doi:10.1016/j.jmr.2005.11.008

treated before. The dynamics of spin-3/2 nuclei under periodic RF irradiation and free precession have been described before only in the context of multiple-pulse quadrupolar echoes [14]. Other previous work has considered the clinical feasibility of SSFP methods but has employed a spin-1/2 model [15].

The purpose of the present study was therefore to investigate the effects that occur with ^{23}Na during SSFP. To minimize the number of degrees of freedom, we have not investigated the influence of imaging gradients on the spatial shape of the steady-state trajectories, but have restricted ourselves to the case of completely balanced SSFP. For reasons stated below, the investigation was done in numerical simulations. Experimental data were acquired to validate the model assumptions. Based on our results, we will also discuss the application potential of SSFP methods.

2. Theory

2.1. Tensor operator formalism

Throughout this work, the density operator σ is expressed in terms of the symmetric ($\hat{T}_{lm}(s)$) and antisymmetric ($\hat{T}_{lm}(a)$) combinations of the unit tensor operators [16]. In this representation σ becomes

$$\sigma = \sum_{l=1}^{3} \sum_{m=-l}^{l} [t_{lm}(s)\hat{T}_{lm}(s) + t_{lm}(a)\hat{T}_{lm}(a)]. \tag{1}$$

The coefficients $t_{lm}(a)$ and $t_{lm}(s)$ are purely real- and imaginary-valued; therefore, magnitude and phase of a pair of coherences $\hat{T}_{lm}(a)$ and $\hat{T}_{lm}(s)$ can be calculated from the complex number $\hat{T}_{lm}(s,a) = \hat{T}_{lm}(a) + \hat{T}_{lm}(s)$. The physical meaning of the tensor operators is: average population ($\hat{T}_{00}$), longitudinal magnetization and Zeeman interaction ($\hat{T}_{10}$), transverse magnetization and interaction with the RF field ($\hat{T}_{11}(s,a)$), quadrupolar polarization and static quadrupolar coupling ($\hat{T}_{20}$), rank-two single quantum coherence ($\hat{T}_{21}(s,a)$), rank-two double quantum coherence ($\hat{T}_{22}(s,a)$), octopolar polarization ($\hat{T}_{30}$), rank-three single quantum coherence ($\hat{T}_{31}(s,a)$), rank-three double quantum coherence ($\hat{T}_{32}(s,a)$), and rank-three triple quantum coherence ($\hat{T}_{33}(s,a)$). In this representation, $\hat{T}_{11}(a)$ and $\hat{T}_{11}(s)$ are the only observable quantities; they correspond to x- and negative y-magnetization, respectively. $\hat{T}_{21}(s,a)$ and $\hat{T}_{31}(s,a)$ are not directly observable but partly evolve into observable $\hat{T}_{11}(s,a)$ through quadrupolar relaxation.

The spin Hamiltonian consists of a Zeeman term (H_Ω), a term expressing the interaction with the radio frequency magnetic field (H_P), and a term which takes quadrupolar interaction into account (H_Q):

$$H = H_\Omega + H_P + H_Q. \tag{2}$$

In the Larmor frequency (ω_0) rotating frame, the Zeeman term and the term for an RF pulse applied along the y-axis are [16]

$$H_\Omega = (\gamma B - \omega_0)\sqrt{5}\hat{T}_{10} = \omega\sqrt{5}\hat{T}_{10}, \tag{3}$$

$$H_P = \omega_1\sqrt{5}\hat{T}_{11}(s). \tag{4}$$

B is the magnetic field at the location of the nucleus. The quadrupolar interaction term consists of a static part

$$H_{QS} = \omega_Q\hat{T}_{20}, \tag{5}$$

which causes a shift of the energy levels [17], and a fluctuating part, which gives rise to relaxation [17,18]. The latter part is not explicitly stated here since it involves a more complex treatment [18]. The formalism for calculating the evolution of σ in the presence of the above-mentioned interactions has been derived before [16–19,22] and will not be described here in detail.

For practical reasons, all coherences are summarized in a 15-element vector:

$$\begin{aligned}\sigma = \{&\hat{T}_{10}, \hat{T}_{11}(s), \hat{T}_{11}(a), \hat{T}_{20}, \hat{T}_{21}(s), \hat{T}_{21}(a),\\ &\hat{T}_{22}(s), \hat{T}_{22}(a), \hat{T}_{30}, \hat{T}_{31}(s),\\ &\hat{T}_{31}(a), \hat{T}_{32}(s), \hat{T}_{32}(a), \hat{T}_{33}(s), \hat{T}_{33}(a)\}^{\mathrm{T}}.\end{aligned} \tag{6}$$

Due to the linear nature of the tensor operator formalism, an evolution of the density operator can be expressed in terms of matrix operations (matrices $\mathbf{M}$ are noted here in boldface). Thus, Larmor precession (or chemical shift) by an angle φ is expressed as

$$\sigma \rightarrow \mathbf{\Omega}(\varphi)\sigma. \tag{7}$$

An RF pulse with flip angle α irradiated along the y-axis is written as

$$\sigma \rightarrow \mathbf{P}(\alpha)\sigma, \tag{8}$$

while an RF pulse applied along an arbitrary axis in the xy-plane, forming an angle φ with the y-axis, takes the form

$$\sigma \rightarrow \mathbf{\Omega}(\varphi)\mathbf{P}(\alpha)\mathbf{\Omega}(-\varphi)\sigma \tag{9}$$

It has been assumed here that the RF pulse is sufficiently short and strong, such that off-resonance effects and effects due to relaxation can be neglected. Finally, quadrupolar relaxation is expressed as

$$\sigma \rightarrow \mathbf{R}(\omega_Q, t)[\sigma - \sigma_0] + \sigma_0. \tag{10}$$

Here $\mathbf{\Omega}$, $\mathbf{P}$, and $\mathbf{R}$ are 15×15 matrices; their explicit form is given in Appendix A. $\sigma_0 = \{\sqrt{5}, \ldots, 0\}^{\mathrm{T}}$ is the equilibrium magnetization.

2.2. Density operator in a balanced SSFP sequence

An SSFP sequence (Fig. 1) consists of an arbitrarily long train of short, phase coherent RF pulses (flip angle α, phase φ) separated by an interpulse delay TR, during which Larmor precession and quadrupolar relaxation determine the evolution of the spin system. φ may progress linearly with the number n of RF pulses, $\varphi_n = n \cdot \Delta\varphi$. The effects of Larmor precession between two consecutive RF pulses and the phase increment $\Delta\varphi$ can be summarized in a single parameter,

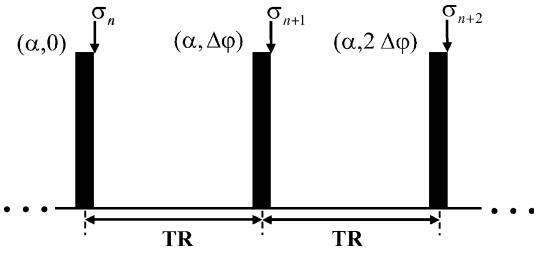

Fig. 1. Schematic representation of an SSFP sequence.

$$\beta = \Delta\varphi - \omega TR, \tag{11}$$

which describes the net precession with respect to the RF pulse phase. The minus sign expresses the fact that spins which precess with the same phase increment per TR as the RF pulse phase are equivalent to on-resonant spins in a sequence with a zero RF pulse phase increment. In particular, the difference between a sequence with a constant ($\varphi = 0, 0, \ldots$) and an alternating RF pulse phase ($\varphi = 0, \pi, \ldots$) just corresponds to a shift of β by π. Now let σ_n represent the density operator immediately after application of the nth RF pulse. The operation transferring the spin system from σ_n to σ_{n+1} involves quadrupolar relaxation, chemical shift, and RF irradiation. Hence σ_{n+1} is given by

$$\sigma_{n+1} = \mathbf{P}(\alpha)\mathbf{\Omega}(\beta)[\mathbf{R}(\omega_Q, TR)[\sigma_n - \sigma_0] + \sigma_0]. \tag{12}$$

For the system to be in the steady state, the condition must be met that the density operator be periodic with the excitation pattern, which means $\sigma_{n+1} = \sigma_n := \sigma_{ss}$, or

$$\sigma_{ss} = \mathbf{P}(\alpha)\mathbf{\Omega}(\beta)[\mathbf{R}(\omega_Q, TR)[\sigma_{ss} - \sigma_0] + \sigma_0]. \tag{13}$$

This system of linear equations, where σ_{ss} is the unknown quantity, are formally independent of the spin number I. An analytical solution can be obtained for $I = 1/2$ [13]. That solution also applies to spin-3/2–nuclei in the extreme narrowing-limit, i.e., if transverse relaxation is quasi-monoexponential. In that case, only tensor operators of rank 1 are different from zero, and the dynamics of ^{23}Na can be described by the Bloch equations. However, with biexponential relaxation present, in an on-resonant system nine coherences are excited, and in a system which is allowed to precess ($\beta \neq 0$), the full set of 15 coherences is excited. An analytical solution has been obtained by solving Eq. (13). This involves straightforward linear algebra and has been done in the Mathematica software (Wolfram Research Inc.). Nevertheless, the resulting expressions are sparse and not very instructive. We do not exclude that there might be shorter expressions, but omitted this and decided to take a numerical approach (see Section 3).

We should also note that the application of imaging gradients switched between the RF pulses does not affect the response of the coherences to α, β, and TR, provided that the gradients are completely balanced,

$$\int_{t=0}^{TR} G(t)\,\mathrm{d}t = 0, \tag{14}$$

where $G(t)$ is the gradient shape. The reason is that with a completely rewinded gradient, the net phase that is accumulated between two RF pulses is zero, regardless of the quantum number m. This, of course, is no longer the case if the condition in Eq. (14) is not fulfilled.

2.3. Measurement of the multiple quantum coherences

In this section we describe a method to measure the coherences $\hat{T}_{lm}(s,a)$ after some preparation, separated according to their quantum number m. The preparation is arbitrary; in this concrete case, of course, it will be an SSFP preparation. By calculation of the observable signal, expressions which link the numerical simulations and experimental results are provided.

Immediately after the preparation, a 90° pulse is applied, the phase of which is stepped through the values $2\pi/12,\ 4\pi/12, \ldots, 2\pi$. The observable signal is calculated with the tensor operator formalism; it can be written in the form

$$S(t,\phi) = \mathrm{e}^{-\mathrm{i}\phi} \sum_{m=-3}^{3} S_m(t)\mathrm{e}^{m\mathrm{i}\phi} \quad m = -3, \ldots, 3. \tag{15}$$

The signal contribution $S_m(t)$, which is obtained by Fourier transformation of $S(t,\phi)$ with respect to ϕ, arises only from $|m|$-quantum coherences,

$$S_m(t) = \theta(t) \sum_{l=|m|}^{3} a_{lm}(t)[\hat{T}_{lm}(a) + \mathrm{sign}(m)\hat{T}_{lm}(s)] \quad \text{for} \tag{16}$$

$$m \epsilon [-3, 3] \setminus 0, \ \text{and} \tag{17}$$

$$S_0(t) = \theta(t)[a_{10}(t)\hat{T}_{10} + a_{20}(t)\hat{T}_{20} + a_{30}(t)\hat{T}_{30}]. \tag{18}$$

Here, $\theta(t)$ represents the Heaviside function, taking into account that signal acquisition starts at $t = 0$. The time dependence due to relaxation is contained in the coefficients $a_{lm}(t)$, which are of the form $a_{lm}(t) = \tilde{a}_{lm} q^1_{1l}(t)$. The factors $\tilde{a}_{lm}$ and the relaxation functions $q^m_{l'l}$ are provided in Appendix A.

It can be found that $a_{l,-m} = -a^*_{l,m}$. Using additionally that the entries for $\hat{T}_{lm}(a)$ and $\hat{T}_{lm}(s)$ are purely real- and imaginary-valued, respectively, it can be shown that

$$S_{-m}(t) = -(S_m(t))^*. \tag{19}$$

In a real sample the quadrupolar frequency is distributed according to a function $\rho(\omega_Q)$ which in a first approximation is assumed to be Gaussian with mean $\bar{\omega}_Q$ and variance σ [18,21],

$$\rho(\omega_Q) \propto \exp(-(\omega_Q - \bar{\omega}_Q)^2/(2\sigma^2)). \tag{20}$$

This is accounted for by considering the NMR signal to be the sum of the contributions originating from different values of ω_Q:

$$S = \int \mathrm{d}\omega_Q S(\omega_Q)\rho(\omega_Q). \tag{21}$$

In the presence of B_0-inhomogeneities, $S_m(t)$ becomes

$$S_m(t) = \theta(t) \int \mathrm{d}\omega_Q \rho(\omega_Q) \sum_{l=|m|}^{3} a_{lm}(t) \times \int \mathrm{d}\omega \mathrm{e}^{\mathrm{i}\omega t} f(\omega) \times [\hat{T}_{l|m|}(a) + \mathrm{sign}(m)\hat{T}_{l|m|}(s)], \quad (22)$$

where $f(\omega)$ represents the distribution of the resonance frequency. $\hat{T}_{l|m|}(a)$ and $\hat{T}_{l|m|}(s)$, as well, depend on ω. The information contained in $S_m(t)$ and $S_{-m}(t)$ can be combined to eliminate $\theta(t)$, using the relation in Eq. (19):

$$\begin{aligned} S_m(t) - (S_{-m}(-t))^* &= \int \mathrm{d}\omega_Q \rho(\omega_Q) \sum_{l=|m|}^{3} (a_{lm}(t)\theta(t) \\ &\quad + a_{lm}(-t)\theta(-t)) \\ &\quad \times \int \mathrm{d}\omega \mathrm{e}^{\mathrm{i}\omega t} f(\omega) \big(\hat{T}_{lm}(a) + \hat{T}_{lm}(s)\big) \\ &= \int \mathrm{d}\omega_Q \rho(\omega_Q) \sum_{l=|m|}^{3} a_{lm}(|t|) \\ &\quad \times \int \mathrm{d}\omega \mathrm{e}^{\mathrm{i}\omega t} f(\omega) \big(\hat{T}_{lm}(a) + \hat{T}_{lm}(s)\big). \end{aligned} \quad (23)$$

Performing the Fourier transformation of the left-hand side in Eq. (23) with respect to t yields a sum of the integrands $f(\omega)(\hat{T}_{lm}(a) + \hat{T}_{lm}(s))$, convolved with the corresponding transverse relaxation functions and implying integration over ω_Q. Note that in the expression in Eq. (23) m ranges only from 0 to 3. The spectral amplitude can be used as a measure for the m-quantum coherences and allows a comparison between simulations and experiment.

3. Methods

3.1. Numerical simulations

The spin operator formalism was implemented as a set of Mathematica (Wolfram Research Inc.) subroutines. σ was written as a 15-element vector, and Larmor precession, RF pulses, and quadrupolar relaxation were implemented as matrix operations acting on σ (see Section 2). Starting from equilibrium magnetization, the iteration was carried out according to Eq. (12). The relative distance in coherence space was measured with the formula

$$d_n = \frac{|\sigma_{n+1} - \sigma_n|}{|\sigma_n|}. \quad (24)$$

Iterations were abandoned when d_n was smaller than 10^{-4}, and σ_{ss} was set to σ_n.

Two different sets of sample-dependent parameters, i.e., relaxation times and mean and variance of the quadrupolar frequency distribution, were used in the simulations. For convenience they are summarized in Table 1. Set A contained the parameters which characterize the agar-phantom used in this work (see Section 4). Since these values were found to be atypical for in vivo samples, a second set of parameters (set B) was used: $T_{2f} = 2$ ms, $T_{2s} = 17$ ms, $T_{1f} = 10$ ms, and $T_{1s} = 52$ ms. The actual T_{2f} and T_{2s} resemble those reported for intracellular sodium in [23,24]. T_{1f} and T_{1s} have been estimated based on a Lorentzian form of the spectral density function $J(\omega)$. Values of ω_Q are annotated with the results. A distribution of the quadrupolar frequency was considered only in one case (see Section 4).

Table 1
Sample-dependent simulation parameters

Set	T_{1f} [ms]	T_{1s} [ms]	T_{2f} [ms]	T_{2s} [ms]	σ [rad/s]	$\bar{\omega}_Q$ [rad/s]
A	36.9	37.0	9.9	37.0	58	132
B	10.0	52.0	2.0	17.0	0, 750	Variable

Sample-dependent simulation parameters. See text for further details.

To compare simulations and experiment, spectra corresponding to the right-hand side in Eq. (23) were computed in simulations with parameter set A. The T_{lm} values in the steady state were multiplied in the frequency domain by $f(\omega) = \exp(-\omega^2/2\Delta\omega^2)$. $\Delta\omega$ was estimated from a global spectrum and T_2-data and was $\Delta\omega/2\pi = 2.4$ Hz. The spectral domain was then inversely Fourier transformed, multiplied by the corresponding coefficients $a_{lm}(t)$, summed and Fourier transformed. Signals were computed at 21 different values of ω_Q, which were equidistantly distributed between $\bar{\omega}_Q - 3\sigma$ and $\bar{\omega}_Q + 3\sigma$. These signals were correspondingly multiplied by $\rho(\omega_Q)$ and summed. The spectral maximum was taken as a measure for the intensity of the multiple quantum spectra.

Simulations with parameter set B yielded a set of $\hat{T}_{lm}(s,a)$ in the steady state for various values of TR, α, and β. The time domain signal was computed by multiplication of $\hat{T}_{11}(s,a)$, $\hat{T}_{21}(s,a)$, and $\hat{T}_{31}(s,a)$ in the β-domain with a Gaussian weighting function ($\Delta\omega/2\pi = 15$ Hz) and subsequent inverse Fourier transformation. The corresponding contributions were then multiplied by the relaxation functions $q^1_{11}(t)$, $q^1_{12}(t)$, and $q^1_{13}(t)$, respectively, and added. Furthermore, as a measure for the overall signal, all points in the time domain signal were summed; this is equivalent to the spectral amplitude. To investigate the dependence of this quantity on β, the $\hat{T}_{11}(s,a)$, $\hat{T}_{21}(s,a)$, and $\hat{T}_{31}(s,a)$ coherences were shifted in the β-domain prior to multiplication with $f(\omega)$.

3.2. NMR experiments

NMR experiments were performed on an 11.75 T Avance 500 spectrometer (Bruker Biospin, Ettlingen, Germany). An approximately spherically-shaped phantom with a diameter of ca. 0.7 mm was fabricated. It consisted of water, 5 vol% agar-agar, and sodium chloride at a 1 M concentration. The agar sphere was encased in a thin latex foil, which was placed in the center of a 20 mL syringe filled with distilled water. The water surrounding the sample served to reduce B_0-inhomogeneities, while the latex-foil prevented diffusion of sodium ions between the

agar-sample and water. This setup was placed in the center of a 20 mm inner diameter birdcage resonator. Due to the small sample size, the B_1 field was practically homogeneous over the entire sample; the duration of a 90° pulse was 50 μs.

3.2.1. Determination of the sample properties

Longitudinal relaxation times T_{1f} and T_{1s} were determined with a triple quantum-filtered inversion-recovery method [22]:

$$(\pi,0)-\tau-\left(\frac{\pi}{2},\phi\right)-\left(\frac{\pi}{2},0\right)-\text{Readout}(t). \tag{25}$$

For each preparation time τ, the pulse phase ϕ was stepped through the values 30°, 90°, 150°, 210°, 270°, and 330°, while the receiver phase was kept constant at 0°. τ took 16 values ranging from 2 to 300 ms. In the time domain, 512 complex data points were read out with a bandwidth of 5 kHz; 16 averages were performed. The signal was Fourier transformed with respect to t and ϕ, resulting in a separation of the components modulated by $\exp(mi\phi)$. The triple quantum (TQ, $m=\pm3$) spectral amplitude assumes the form

$$S_{\pm3}(\tau)\propto(e^{-\tau/T_{1f}}-e^{-\tau/T_{1s}})(T_{2f}-T_{2s}), \tag{26}$$

whereas the single quantum (SQ, $m=\pm1$) spectral amplitude can be written as

$$S_{\pm1}(\tau)\propto -8\left(1-\frac{2}{5}e^{-\tau/T_{1f}}-\frac{8}{5}e^{-\tau/T_{1s}}\right)(3T_{2f}+2T_{2s}) + \frac{6\sqrt{6}}{25}(e^{-\tau/T_{1f}}-e^{-\tau/T_{1s}})(T_{2f}-T_{2s}). \tag{27}$$

For the sample used here, T_{1f} and T_{1s} were very close to each other, indicated by a low TQ signal. Both values were therefore obtained by nonlinear fit to the SQ signal, neglecting the transient-shaped term (second summand in Eq. (27); see also Section 5). Spectral densities at one and two times the Larmor frequency were computed using the expressions

$$J_1=J(\omega_0)=\frac{1}{2T_{1f}}, \tag{28}$$

$$J_2=J(2\omega_0)=\frac{1}{2T_{1s}}. \tag{29}$$

The short transverse relaxation time T_{2f} was measured with a double quantum magic angle (DQ-MA) pulse sequence [18]:

$$(\pi/2,\phi)-\tau/2-(\pi,\phi)-\tau/2-(\theta_m,\phi-\pi/2)-\delta-(\theta_m,0). \tag{30}$$

For each τ, the pulse phase ϕ was stepped through the values 0°, 90°, 180°, and 270°, while the receiver phase alternated between 0° and 180°. The experiment was performed using 16 values of τ in the range from 960 μs to 40 ms; the evolution time δ was kept very short (60 μs). In the time domain, 512 complex data points were read out with a 5 kHz bandwidth, and 16 averages were performed. The four FIDs were added to obtain the double quantum signal. Assuming a Gaussian distribution of the quadrupolar frequency, the double quantum signal takes the form [18]

$$S_{\mathrm{DQ}}\propto[e^{-\sigma^2(t-\tau)^2/2}\cos(\bar{\omega}_Q(t-\tau))-e^{-\sigma^2(t+\tau)^2/2} \times\cos(\bar{\omega}_Q(t+\tau))]\times e^{-t/T_{2f}}e^{-t/T_{2s}}. \tag{31}$$

This function was fit to the data in the t and τ domain using a two-dimensional, nonlinear fit (Levenberg–Marquard-algorithm) to obtain T_{2f}, $\bar{\omega}_Q$, and σ. The spectral density at frequency zero was computed with the formula

$$J_0=J(0)=\frac{1}{T_{2f}}-J_1-J_2. \tag{32}$$

3.2.2. Measurement of the single, double, and triple quantum coherences in the steady state

The pulse sequence used to measure the single, double, and triple quantum coherences in the steady state consisted of an SSFP preparation block (33 pulses, TR = 12 ms, $\alpha=45°$ and 72°, phase increment $\Delta\varphi$) followed by a (90°, ϕ) coherence transfer pulse and data acquisition (512 complex data points, bandwidth 5 kHz). The experiment was performed for 32 values of $\Delta\varphi$ equidistantly distributed in the range $[-\pi,\pi]$. In another series of measurements, the flip angle was varied in 19 steps between 9° and 171° for $\Delta\varphi=\pi$. In each experiment, the coherence transfer pulse phase was stepped through the values $\phi=k\cdot 2\pi/12$, $k=0,\ldots,11$. The whole preparation block was 384 ms long, which is about ten times the T_1 of the sample. This ensured that the system had converged to the steady state at the end of the preparation block. The maximal RF duty cycle was 0.8%.

After phase correction, the data were Fourier transformed in the ϕ direction, and m-quantum spectra were computed as described in the Section 2. The spectral maximum was taken for the comparison between simulations and experiment.

4. Results

4.1. Sample properties

Measurement of the longitudinal relaxation times yielded $T_{1f}=36.9\pm0.5$ ms and $T_{1s}=37.0\pm0.5$ ms. Spectral densities J_1 and J_2 were computed to be 13.6 and 13.5 s^{-1}, respectively. Using Eq. (A.7) T_{2s} was determined to be 37.0 ms. Results of the DQ-MA method were $T_{2f}=9.9\pm0.3$ ms, $\bar{\omega}_Q=132\pm3$ rad/s and $\sigma=58\pm3$ rad/s. The spectral density J_0 was calculated to be 73.9 s^{-1}.

4.2. Comparison between simulations and experiment

Simulated and experimentally measured spectral amplitudes are plotted together in Fig. 2. SQ, DQ, and TQ signals have been normalized to the SQ signal acquired after a single 90° excitation pulse. The qualitative shape of the experimental data curves is reproduced in the simulations, except for slight deviations of the DQ signal (B) around $\beta=\pi$. Good quantitative agreement between simulations

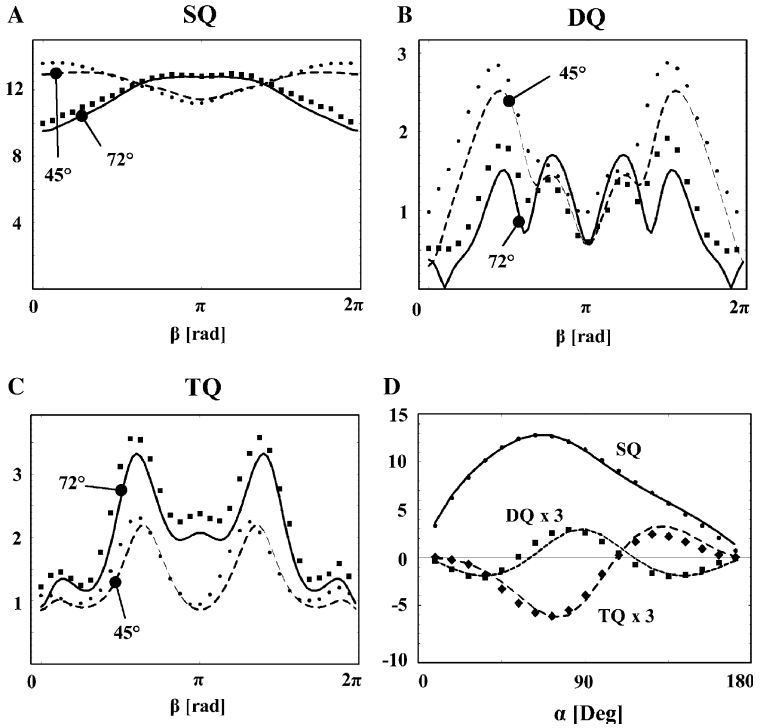

Fig. 2. Comparison between simulated and experimental data (lines and symbols, respectively). Shown are the single (SQ), double (DQ), and triple quantum (TQ) signals as a function of β (A–C) and α (D). (A–C) Experimental data at 45° and 72° are denoted by ● and ■, respectively. (D) The SQ, DQ, and TQ signals are denoted by ●, ♦, and ■, respectively. In (D) the DQ and TQ signals have been multiplied by 3 to fit to the scale of the SQ signal. The TR was 12 ms. Sample and simulation parameters are given in Section 4.

and experiment has been achieved for the SQ signal at $\beta = \pi$ (A and D).

4.3. Study of the dynamics with parameter set B

The steady-state values of the $\hat{T}_{lm}(s,a)$ coherences show a behavior which is periodic in ω_Q. This is illustrated in Fig. 3 for the single quantum coherences ($\hat{T}_{11}(s,a)$, $\hat{T}_{21}(s,a)$, and $\hat{T}_{31}(s,a)$) and is a simple consequence of the fact that the relaxation functions $q^m_{l'l}$ themselves are periodic with ω_Q. The amplitude of the oscillations increases with decreasing TR. While $\hat{T}_{21}(s,a)$ is dominated by these oscillations—depending on ω_Q, $\hat{T}_{21}(s,a)$ can be zero or maximally excited—the influence of ω_Q on $\hat{T}_{11}(s,a)$ and $\hat{T}_{31}(s,a)$ is less pronounced.

In Fig. 4 the single quantum coherences are plotted as a function of the flip angle for an alternating RF pulse phase ($\beta = \pi$). The influence of ω_Q can be best observed at short TR and is therefore only shown at TR = 4 ms. Remarkably, there are flip angles at which $\hat{T}_{11}(s,a)$, $\hat{T}_{21}(s,a)$ or $\hat{T}_{31}(s,a)$ are zero.

We focus now on the flip angle around which $\hat{T}_{31}(s,a)$ is nearly maximally excited, $\alpha = 72°$. Magnitude and phase of the single quantum coherences are shown as a function of β in Fig. 5. At TR = 12 ms, the shape of the $\hat{T}_{11}(s,a)$ magnitude profile resembles that of spin-1/2 nuclei, but at shorter TR an additional mode at $\beta = \pi$ becomes visible. With decreasing TR, the $\hat{T}_{11}(s,a)$ phase profile becomes less flat, and the average slope around $\beta = \pi$ becomes steeper. $\hat{T}_{21}(s,a)$ is about one order of magnitude lower than $\hat{T}_{31}(s,a)$. The $\hat{T}_{31}(s,a)$ magnitude profile is composed of three modes which become more distinct at shorter TR.

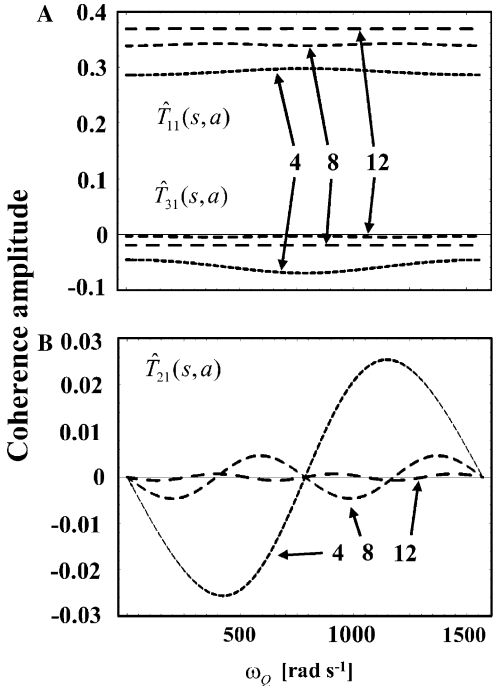

Fig. 3. Effect of ω_Q on $\hat{T}_{11}(s,a)$, $\hat{T}_{21}(s,a)$ (A), and $\hat{T}_{21}(s,a)$ (B). Graphs are shown for TR = 4, 8, and 12 ms (annotated in the graphs). Further sequence parameters were α= 30° and $\beta = \pi$. Sample parameters: set B.

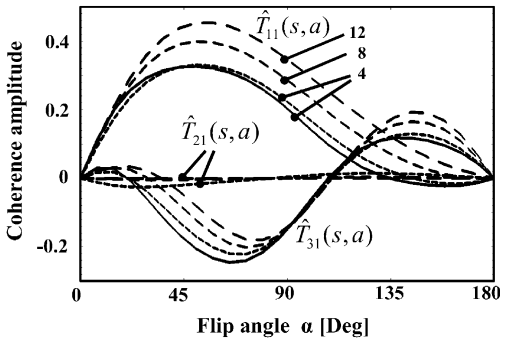

Fig. 4. Simulated dependence of $\hat{T}_{11}(s,a)$, $\hat{T}_{21}(s,a)$, and $\hat{T}_{31}(s,a)$ on the flip angle, for various TR (4, 8, and 12 ms) and $\beta = \pi$. For the graphs showing $\hat{T}_{11}(s,a)$ and $\hat{T}_{31}(s,a)$, ω_Q has been set to zero (dashed lines) and π/TR (solid lines). For the $\hat{T}_{21}(s,a)$ curves, ω_Q has been set to $\pi/(2\,\mathrm{TR})$. Sample parameters: set B.

The $\hat{T}_{31}(s,a)$ phase spans a range from 0 to 2π, for other flip angles also from -2π to 0 (not shown). At TR = 4 ms, changes in ω_Q have an effect on the magnitude and phase profiles of the single quantum coherences, while at TR = 8 and 12 ms the curves for different ω_Q are practically identical.

The course of the single quantum coherences in the β-domain results in an observable time domain signal which is shown in Fig. 6. It has been plotted for the shortest (A,C) and longest TR (B,D) and for two values of ω_Q for which $\hat{T}_{21}(s,a)$ is minimally and maximally excited, respectively. Signal decay caused purely by off-resonances has been denoted by a prime. The total signal is dominated by the contribution of $\hat{T}_{11}(s,a)$; the ratio of the contributions $\hat{T}_{31}(s,a)$ versus $\hat{T}_{11}(s,a)$, however, is larger at the shorter TR. The $\hat{T}'_{11}(s,a)$ signal has a maximum at $t \approx 2$ ms, both for TR = 4 and 12 ms. At both values of TR the $\hat{T}'_{31}(s,a)$ signal is maximal at $t = 0$, indicating defocusing behavior. The signal contribution originating from $\hat{T}_{21}(s,a)$ is practically zero. Differences in the time domain signal between (A,B) and (C,D) are mainly due to the different shape of the relaxation functions $q^1_{11}(\omega_Q,t)$ and $q^1_{13}(\omega_Q,t)$.

The dependence of $\hat{T}_{11}(s,a)$, $\hat{T}_{21}(s,a)$, and $\hat{T}_{31}(s,a)$ on TR is shown in Fig. 7. With increasing TR, $\hat{T}_{11}(s,a)$ decreases, while $\hat{T}_{21}(s,a)$ and $\hat{T}_{31}(s,a)$ increase.

One consequence of the excitation of multiple quantum coherences in the steady state is that the amplitude ratio of the fast versus the slowly decaying components deviates from the usual value 3:2. The observable signal is given by the single quantum coherences immediately after the RF pulse:

$$S(t) = \sum_{l=1}^{3} q^1_{1l}(t)[\hat{T}_{lm}(a) + \hat{T}_{lm}(s)]. \tag{33}$$

Arranging the terms in Eq. (33) which contain the fast and slow relaxation rates, it can be recognized that these depend differently on the single quantum coherences:

$$\begin{aligned} FC_{1,3}(t) = \Bigg[& \frac{3}{10}\left(1 \pm \frac{J_2}{\sqrt{J_2^2 - \omega_Q^2}}\right)\hat{T}_{11}(s,a) \\ & \mp \frac{\mathrm{i}}{2}\sqrt{\frac{3}{5}}\frac{\omega_Q}{\sqrt{J_2^- \omega_Q^2}}\hat{T}_{21}(s,a) \\ & + \frac{\sqrt{6}}{10}\left(1 \pm \frac{J_2}{\sqrt{J_2^2 - \omega_Q^2}}\right)\hat{T}_{31}(s,a)\Bigg] \exp(-R^1_{1,3}t), \end{aligned} \tag{34}$$

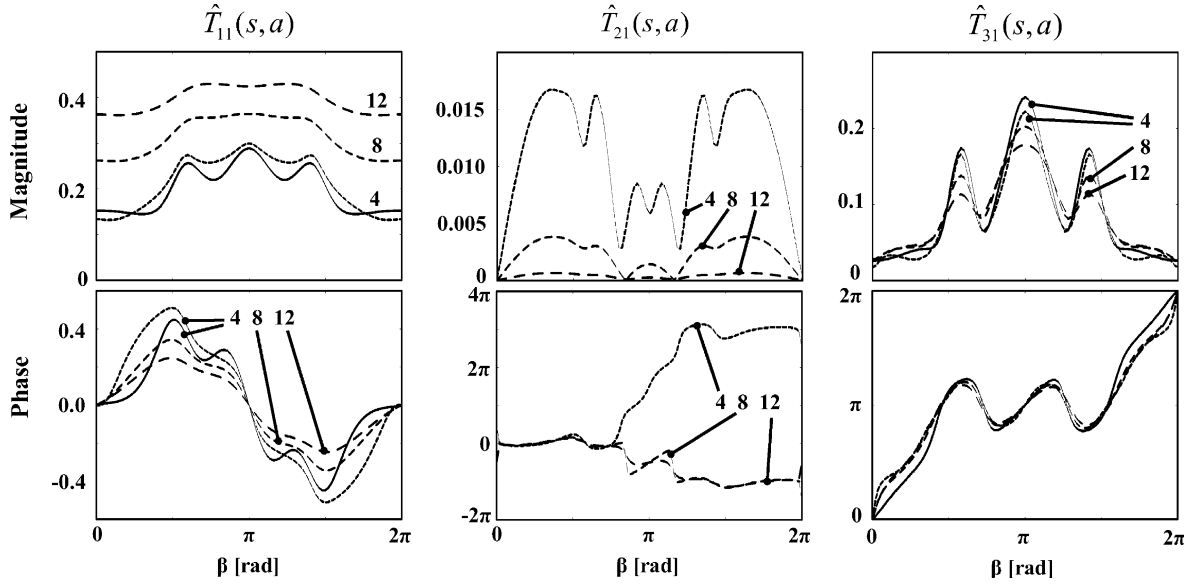

Fig. 5. Simulated $\hat{T}_{11}(s,a)$ (left column), $\hat{T}_{21}(s,a)$ (middle column), and $\hat{T}_{31}(s,a)$ (right column) as a function of β, at $\alpha = 72°$ and TR = 4, 8, and 12 ms (annotated with the graphs). The graphs showing $\hat{T}_{11}(s,a)$ and $\hat{T}_{31}(s,a)$ have been obtained with $\omega_Q = 0$ (dashed lines) and $\omega_Q = \pi$/TR (solid lines). The $\hat{T}_{21}(s,a)$ curves shown here have been obtained for $\omega_Q = \pi/(2\,\mathrm{TR})$. Sample parameters: set B.

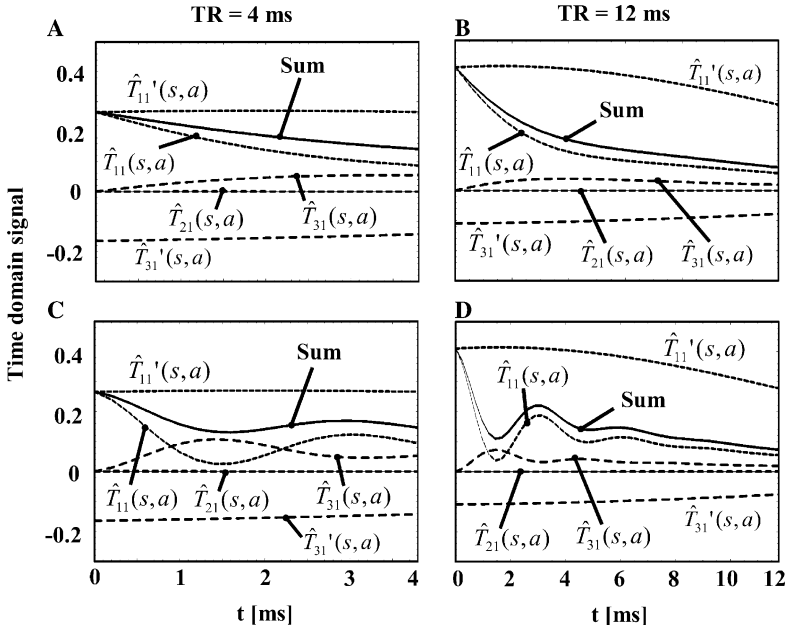

Fig. 6. Simulated time domain signal (solid lines) and its contributions from $\hat{T}_{11}(s,a)$, $\hat{T}_{21}(s,a)$, and $\hat{T}_{31}(s,a)$ (dashed lines). Signal decay caused by off-resonances has been denoted by $\hat{T}'_{11}(s,a)$, etc., ω_Q is 0 (A,B) and 393 s^{-1} (C,D), such that $\hat{T}_{21}(s,a)$ is maximally excited. Sample parameters: set B.

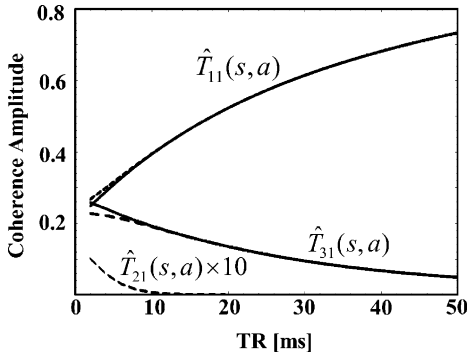

Fig. 7. $\hat{T}_{11}(s,a)$, $\hat{T}_{21}(s,a)$, and $\hat{T}_{31}(s,a)$ as a function of TR, for $\beta = \pi$ and $\alpha = 72°$. For the graphs showing $\hat{T}_{11}(s,a)$ and $\hat{T}_{31}(s,a)$ ω_Q has been set to zero (dashed lines) and π/TR (solid lines). The curve showing $\hat{T}_{21}(s,a)$ was obtained with $\omega_Q = \pi/(2\ \mathrm{TR})$; it has been multiplied by a factor 10. Sample parameters: set B.

$$SC(t) = \left[\frac{2}{5}\hat{T}_{11}(s,a) - \frac{\sqrt{6}}{5}\hat{T}_{31}(s,a)\right]\exp(-t/T_{2s}). \qquad (35)$$

If J_2 is small compared to J_0, the real parts of R_1^1 and R_3^1 are not very different, and from a practical point of view it makes sense to summarize the two fast decaying components $FC_1(t)$ and $FC_3(t)$ in a single fast decaying component, $FC(t) = FC_1(t) + FC_3(t)$. Since $\hat{T}_{11}(s,a)$, $\hat{T}_{21}(s,a)$, and $\hat{T}_{31}(s,a)$ depend differently on the sequence parameters (α, β, and TR), the fast and slowly decaying components do so as well. The dependence on β is illustrated in Fig. 8. At $\beta = \pi$ the slowly decaying component contributes more to the overall signal, while around $\beta = 0$ the fast decaying component is dominant. Note that not only the amplitude, but also the phase (Fig. 8B) of the fast and slowly decaying components behave differently. The relative signal amplitude of the slowly decaying component, $\eta = SC(0)/[SC(0) + FC(0)]$, is plotted in Fig. 9. In this graph the influence of off-resonance effects has already been included by integration over β using the same Gaussian distribution as for calculating the time domain signals. For a sequence with alternating RF pulse phase ($\beta = \pi$) η is approximately

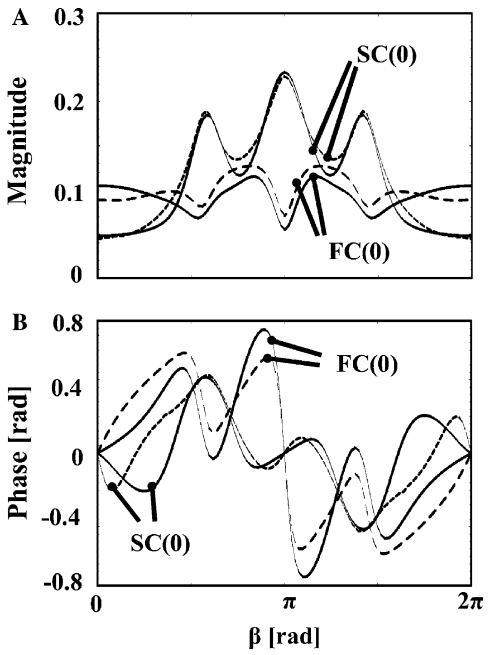

Fig. 8. Magnitude (A) and phase (B) of the fast (FC) and slowly decaying signal components (SC) computed according to Eqs. (34) and (35). Sequence parameters are $\alpha = 72°$ and TR = 4 ms. Curves are shown for $\omega_Q = 0$ (dashed lines) and $\omega_Q = \pi/\mathrm{TR}$ (solid lines). Sample parameters: set B.

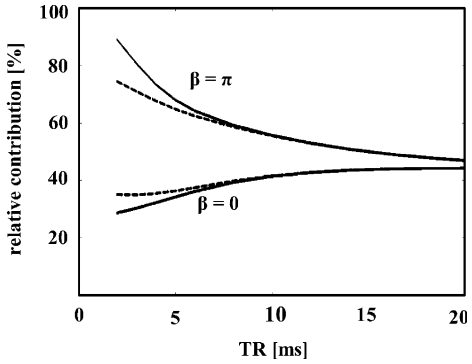

Fig. 9. Contribution of the slowly decaying component to the total signal amplitude, $\eta = SC(0)/(FC(0) + SC(0))$. Effects due to a distribution of the resonance frequency have been included by a Gaussian weighting in the frequency domain. The curves have been computed for $\omega_Q = 0$ (dashed lines) and $\omega_Q = \pi/TR$ (solid lines). Sample parameters: set B.

40% at long TR, but significantly larger at short TR. This effect occurs for any ω_Q, but is maximal for $\omega_Q = \pi/TR$.

The area under the curve (AUC) of the time domain signal is shown in Fig. 10. Values have been divided by TR to allow a comparison between different TR values. The graphs have been obtained by integration over ω_Q using a Gaussian distribution of the quadrupolar frequency with mean $\bar{\omega}_Q = 0$ and variance $\sigma = 750$ rad/s. The latter value for σ has been taken from previously reported measurements in cartilage [18]. Other values of σ were tested as well, but the corresponding curves do not look qualitatively different (not shown). The distribution of the resonance frequency causes blurring of the magnitude and phase profiles. Since the width of the distribution scales inversely with TR, this effect is less pronounced at short TR. Remarkably, at some flip angle (here ca. 135°) the AUC is zero.

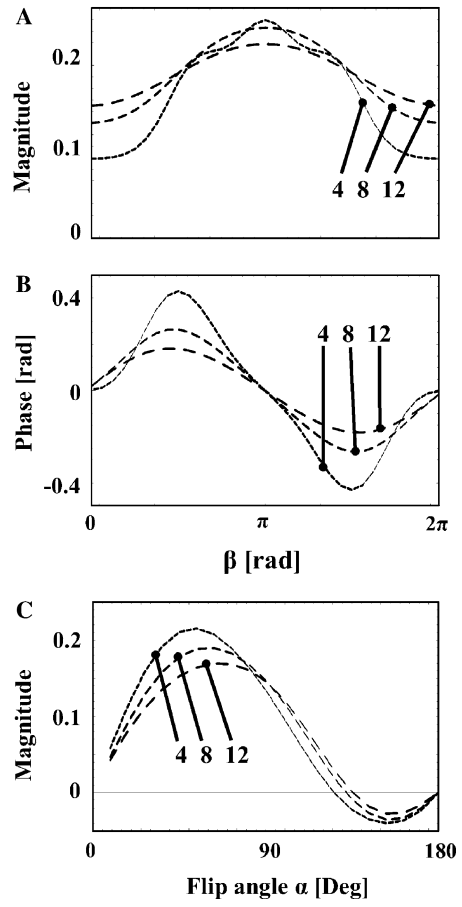

Fig. 10. Total accumulated signal per unit time for various TR = 4, 8, and 12 ms (annotated). In (A) and (B) $\alpha = 72°$, and in (C) $\beta = \pi$. Off-resonance effects have been included by a Gaussian weighting in the frequency domain. Furthermore, integration over ω_Q has been performed using a Gaussian distribution of ω_Q with mean $\bar{\omega}_Q = 0$ and variance $\sigma = 750$ rad/s. Sample parameters: set B.

5. Discussion

5.1. Comparison between simulations and experiment

The behavior of ^{23}Na during SSFP has been investigated in numerical simulations and experiments. Both show that during SSFP multiple quantum coherences are excited. All curves, except for the DQ graphs in Fig. 2B, show good qualitative agreement between simulations and experiment; the latter show at least partial qualitative agreement. For the SQ signal even good quantitative agreement is observed ($\beta = \pi$, Figs. 2A and D). Note that the model curves have not been obtained by some fit procedure, but by measurement of the sample characteristics under certain model assumptions and subsequent simulation.

The deviations between the simulated and experimental data are not limited to a single source. Above all, the sample is certainly composed of a multitude of domains which are characterized by different sets of model parameters. For instance, a nonlinear fit to the triple quantum signal (Eq. (26)) yielded different values of T_{1f} and T_{1s} than those obtained from the single quantum signal (Eq. (27)), with an amplitude corresponding to 2% of the sample. This compartment was neglected in the simulations due to its small partition, but also because its transverse relaxation times could not be determined. Furthermore, it is clear that the approximation of the distributions of ω and ω_Q by a Gaussian is only a rough simplification. Nevertheless, using these simplifications, it is possible to come close to the experimental data, and large computational and experimental effort is avoided.

Eq. (31) is only valid if no essential contributions arise from the range $-J_2 \leqslant \omega_Q \leqslant J_2$, thus if hidden quadrupolar splitting does not play a significant role. In the agar sample used here, this condition is fulfilled to a good approximation: only 1.4% of the total area under curve of $\rho(\omega_Q)$ are between $-J_2$ and J_2.

5.2. Simulations with parameter set B

Quadrupolar relaxation effects during periodic RF irradiation have been described before in the context of multiple-pulse quadrupolar echoes [14]. The latter method can

be considered as the special case $\beta = 0$ of an SSFP sequence. While in that work, the dynamics were considered for $\alpha \approx 90°$ and at a short TR ($\ll T_{2f}$), with the emphasis on relaxation during irradiation, in this work the regime of long TR has been studied. Furthermore, in the present work the investigation could be extended to general α and β.

The simulations have shown that in some regimes of parameter space the observable signal can be approximately described by the Bloch equations. For instance, the trend has been observed that at low flip angles and long TR the curves (magnitude and phase profile in the β-domain, flip angle dependency) are similar to those observed with spin-1/2 nuclei. In this comparison, we exclude biexponential relaxation, which is an effect that can not be explained by the Bloch equations, but in the case of similar T_{1f} and T_{1s} could be artificially introduced by considering two pools that exhibit different relaxation times.

There are other regimes of parameter space—here at short TR and large flip angles—where the excitation of multiple quantum coherences leads to effects which would not occur with dynamics based on the Bloch equations. One example is the occurrence of more than two modes in the magnitude and phase profile (Figs. 5 and 10). Another example is that the total time domain signal is zero at some flip angle between 0° and 180° (here ca. 135°, Fig. 10C). This effect is due to a cancellation of the contributions from $\hat{T}_{11}(s,a)$ and $\hat{T}_{31}(s,a)$. Third, a non-zero mean of the quadrupolar frequency distribution would cause the time domain signal to look similar to those shown in Figs. 6C and D.

At flip angles below ca. 110° and for $\beta = \pi$, $\hat{T}_{31}(s,a)$ becomes larger with shorter TR (Figs. 4 and 7). As a consequence, the relative contribution of the slowly decaying component increases. This effect contributes to the increase of the total accumulated signal per unit time at short TR (Fig. 10), although the latter effect is mainly due to the shorter decay period. A deviation of the 3:2 amplitude ratio of the fast and slowly decaying components, η, has been reported in the context of spin-lock NMR [20,14]. Although the mechanism is different—in spin-lock NMR $T_{1\rho}$ relaxation plays the dominant role—the similar result was found that the fast decaying component is favored for a constant RF pulse phase ($\beta = 0$, Fig. 9). Furthermore, we have shown that this effect is reversed for an alternating pulse phase ($\beta = \pi$), and that η is in general a function of α, β, and TR. The practical importance of this effect is, of course, that the problem of sodium visibility can be reduced using SSFP.

The refocusing properties of SSFP methods can be understood by considering the response of the signal phase to β. This is somewhat more complicated for ^{23}Na because $\hat{T}_{11}(s,a)$ and $\hat{T}_{31}(s,a)$ have different phase profiles and therefore different refocusing properties. It has been observed in the simulations that at a TR that is short compared to the transverse relaxation times, the $\hat{T}_{11}(s,a)$ phase profile has an approximate slope of $-1/2$ around $\beta = \pi$, leading to an echo at TR/2 (TR = 4 ms), in spite of a defocusing $\hat{T}_{31}(s,a)$ phase profile. At larger values of TR, the echo occurs significantly earlier than at TR/2, because TR is much larger than T_{2f} and on the order of T_{2s}. The shape of the time domain signal (Fig. 6) shows, however, that these considerations do not play an important role with ^{23}Na. Transverse signal decay is dominated by—compared to TR—the short T_{2f} and T_{2s}, and the occurrence of an echo-like signal maximum in the signal evolution due to off-resonances can be practically neglected. Therefore, the shortest possible echo times are preferable to obtain optimal SNR.

With sample parameters B and the sequence parameters used here, coherences of rank 2 were excited only to a low extent. Furthermore, variation of ω_Q had only little effect on $\hat{T}_{11}(s,a)$ and $\hat{T}_{31}(s,a)$, and practically no effect at TR = 8 and 12 ms. Both observations can be attributed to the fact that TR was longer than T_{2f}. While the temporal dynamics of $\hat{T}_{11}(s,a)$ and $\hat{T}_{31}(s,a)$ are determined by a short and a long time constant, $\hat{T}_{21}(s,a)$ decays with a single short time constant. SSFP, however, only emphasizes those signal contributions which have a relaxation time that is about equal to or longer than TR. Similarly, those parts of $\hat{T}_{11}(s,a)$ and $\hat{T}_{31}(s,a)$ (and all other coherences) which are sensitive to ω_Q are modulated by fast relaxation as well, and therefore do not contribute to the SSFP-dynamics.

With shorter TR, the RF duty cycle becomes larger, and relaxation during the RF pulse can no longer be neglected. In our hardware setup it was not necessary to take this effect into account because the RF duty cycle was low (0.4% for a 90° pulse), as was the absolute duration of the RF pulses compared to the transverse relaxation times. This situation is different for clinical scanners, with typical RF pulse lengths of 500 μs or 1 ms. A formalism to compute relaxation during the RF pulse is available [18] and could have been included in the calculations. For practical reasons, however, the regime of short TR was not explored in the present work. In this regime, several difficulties occur which make the application of SSFP rather impractical, such as spin heating, high requirements to the imaging gradient system, and SNR loss due to a low ADC duty cycle.

5.3. Outlook: application potential

It has been shown by Kim and Parrish that SSFP methods can be used to acquire in vivo ^{23}Na-images [5,15]. In [5], a sequence optimization was performed with an experimental approach, while in [15] considerations to optimize the image SNR were based on the Bloch equations. We have shown in the present study that for an understanding of the dynamics, the spin-3/2 properties of ^{23}Na must be considered. These play a practical role for the implementation and optimization of ^{23}Na imaging, which suffers from inherently low sensitivity.

Beyond sequence optimization, the results presented here suggest that SSFP could have the potential to differentiate between pools containing Na^+-ions with different mobility or different quadrupolar coupling. This is hitherto only performed by multiple quantum filtration techniques [9,11,22,23]. The latter techniques have the drawback that a long TR is needed, resulting in a rather low SNR per unit time compared to usual (single quantum) imaging methods. During SSFP, multiple quantum coherences are excited and have an effect on the observable signal. Thus, SSFP methods are sensitive to the spin-3/2 properties of ^{23}Na. However, separation of the signal contributions originating from single and multiple quantum coherences is only possible by leaving the steady state, which is not desirable. It remains, therefore, unresolved whether an improvement compared to multiple quantum filters can be achieved using SSFP methods. Nevertheless, it could be instructive to study the signal response with respect to a change of the sequence parameters in a multi-compartment system. This will be subject of future work.

Appendix A. Matrices P, R, and Ω

A.1. RF pulses

RF pulses act in subspaces of σ characterized by the same rank l; $\mathbf{P}$ has therefore block-diagonal shape:

$$\mathbf{P} = \begin{pmatrix} \mathbf{P}_{l=1} & & \\ & \mathbf{P}_{l=2} & \\ & & \mathbf{P}_{l=3} \end{pmatrix}. \tag{A.1}$$

Closed expressions for the matrix elements P_{ij} have been taken from [16]; the sub-matrices are

$$\mathbf{P}_{l=1} = \begin{pmatrix} \cos(\alpha) & 0 & \sin(\alpha) \\ 0 & 1 & 0 \\ -\sin(\alpha) & 0 & \cos(\alpha) \end{pmatrix}, \tag{A.2}$$

$$\mathbf{P}_{l=2} = \begin{pmatrix} \frac{1}{4}(1+3\cos(2\alpha)) & 0 & \frac{\sqrt{3}}{2}\sin(2\alpha) & \frac{\sqrt{3}}{4}(1-\cos(2\alpha)) & 0 \\ 0 & \cos(\alpha) & 0 & 0 & \sin(\alpha) \\ -\frac{\sqrt{3}}{2}\sin(2\alpha) & 0 & \cos(2\alpha) & \frac{1}{2}\sin(2\alpha) & 0 \\ \frac{\sqrt{3}}{4}(1-\cos(2\alpha)) & 0 & -\frac{1}{2}\sin(2\alpha) & \frac{1}{4}(\cos(2\alpha)+3) & 0 \\ 0 & -\sin(\alpha) & 0 & 0 & \cos(\alpha) \end{pmatrix}, \tag{A.3}$$

and

$$\mathbf{P}_{l=3} = \begin{pmatrix} P_{99} & 0 & P_{9b} & P_{9c} & 0 & 0 & P_{9f} \\ 0 & P_{aa} & 0 & 0 & P_{ad} & P_{ae} & 0 \\ P_{b9} & 0 & P_{bb} & P_{bc} & 0 & 0 & P_{bf} \\ P_{c9} & 0 & P_{cb} & P_{cc} & 0 & 0 & P_{cf} \\ 0 & P_{da} & 0 & 0 & P_{dd} & P_{de} & 0 \\ 0 & P_{ea} & 0 & 0 & P_{ed} & P_{ee} & 0 \\ P_{f9} & 0 & P_{fb} & P_{fc} & 0 & 0 & P_{ff} \end{pmatrix}. \tag{A.4}$$

The entries P_{ij} of $\mathbf{P}_{l=3}$ are:

$$\begin{aligned}
P_{99} &= \tfrac{1}{8}(5\cos(3\alpha)+3\cos(\alpha)),\\
P_{9b} &= \tfrac{1}{8}\sqrt{\tfrac{3}{2}}(5\sin(3\alpha)+\sin(\alpha)),\\
P_{9c} &= -\tfrac{\sqrt{15}}{8}(\cos(3\alpha)-\cos(\alpha)),\\
P_{9f} &= -\tfrac{1}{8}\sqrt{\tfrac{5}{2}}(\sin(3\alpha)-3\sin(\alpha)),\\
P_{aa} &= \tfrac{1}{8}(5\cos(2\alpha)+3),\\
P_{ad} &= \tfrac{1}{2}\sqrt{\tfrac{5}{2}}\sin(2\alpha),\\
P_{ae} &= \tfrac{\sqrt{15}}{8}(1-\cos(2\alpha)),\\
P_{b9} &= -P_{9b},\\
P_{bb} &- \tfrac{1}{16}(15\cos(3\alpha)+\cos(\alpha)),\\
P_{bc} &= \tfrac{1}{8}\sqrt{\tfrac{5}{2}}(3\sin(3\alpha)-\sin(\alpha)),\\
P_{bf} &= -\tfrac{\sqrt{15}}{16}(\cos(3\alpha)-\cos(\alpha)),\\
P_{c9} &= P_{9c},\\
P_{cb} &= -P_{bc},\\
P_{cc} &= \tfrac{1}{8}(3\cos(3\alpha)+5\cos(\alpha)),\\
P_{cf} &= \tfrac{1}{8}\sqrt{\tfrac{3}{2}}(\sin(3\alpha)+5\sin(\alpha)),\\
P_{da} &= -P_{ad},\\
P_{dd} &= \cos(2\alpha),\\
P_{de} &= \tfrac{1}{2}\sqrt{\tfrac{3}{2}}\sin(2\alpha),\\
P_{ea} &= P_{ae},\\
P_{ed} &= -P_{de},\\
P_{ee} &= \tfrac{3}{8}\cos(2\alpha)+\tfrac{5}{8},\\
P_{f9} &= -P_{9f},\\
P_{fb} &= P_{bf},\\
P_{fc} &= -P_{cf}, \text{ and}\\
P_{ff} &= \tfrac{1}{16}(\cos(3\alpha)+15\cos(\alpha)).
\end{aligned}$$

A.2. Quadrupolar relaxation

Analogous to RF pulses, quadrupolar relaxation acts in subspaces of σ given by the same quantum number m. Accordingly, the relaxation matrix $\mathbf{R}$ reads

$$\mathbf{R} = \begin{pmatrix}
q_{11}^0 & 0 & 0 & 0 & 0 & 0 & 0 & 0 & q_{13}^0 & 0 & 0 & 0 & 0 & 0 & 0 \\
0 & q_{11}^1 & 0 & 0 & 0 & q_{12}^1 & 0 & 0 & 0 & q_{13}^1 & 0 & 0 & 0 & 0 & 0 \\
0 & 0 & q_{11}^1 & 0 & q_{12}^1 & 0 & 0 & 0 & 0 & 0 & q_{13}^1 & 0 & 0 & 0 & 0 \\
0 & 0 & 0 & q_{22}^0 & 0 & 0 & 0 & 0 & 0 & 0 & 0 & 0 & 0 & 0 & 0 \\
0 & 0 & q_{21}^1 & 0 & q_{22}^1 & 0 & 0 & 0 & 0 & 0 & q_{23}^1 & 0 & 0 & 0 & 0 \\
0 & q_{21}^1 & 0 & 0 & 0 & q_{22}^1 & 0 & 0 & 0 & q_{23}^1 & 0 & 0 & 0 & 0 & 0 \\
0 & 0 & 0 & 0 & 0 & 0 & q_{22}^2 & 0 & 0 & 0 & 0 & 0 & q_{23}^2 & 0 & 0 \\
0 & 0 & 0 & 0 & 0 & 0 & 0 & q_{22}^2 & 0 & 0 & 0 & q_{23}^2 & 0 & 0 & 0 \\
q_{31}^0 & 0 & 0 & 0 & 0 & 0 & 0 & 0 & q_{33}^0 & 0 & 0 & 0 & 0 & 0 & 0 \\
0 & q_{31}^1 & 0 & 0 & 0 & q_{32}^1 & 0 & 0 & 0 & q_{33}^1 & 0 & 0 & 0 & 0 & 0 \\
0 & 0 & q_{31}^1 & 0 & q_{32}^1 & 0 & 0 & 0 & 0 & 0 & q_{33}^1 & 0 & 0 & 0 & 0 \\
0 & 0 & 0 & 0 & 0 & 0 & 0 & q_{32}^2 & 0 & 0 & 0 & 0 & q_{33}^2 & 0 & 0 \\
0 & 0 & 0 & 0 & 0 & 0 & q_{32}^2 & 0 & 0 & 0 & 0 & 0 & 0 & q_{33}^2 & 0 \\
0 & 0 & 0 & 0 & 0 & 0 & 0 & 0 & 0 & 0 & 0 & 0 & 0 & 0 & q_{33}^3 \\
0 & 0 & 0 & 0 & 0 & 0 & 0 & 0 & 0 & 0 & 0 & 0 & 0 & 0 & q_{33}^3
\end{pmatrix}. \tag{A.5}$$

Explicit expressions for the relaxation functions $q_{l'l}^m$ in a zero-average electric field gradient have been provided in [22]; this has been extended to the case of non-zero average electric field gradients in [17,19]. The non-zero relaxation functions are

$$
\begin{aligned}
q^0_{11}(t) =& 1/5[4\exp(-t/T_{1s}) + \exp(-t/T_{1f})],\\
q^0_{13}(t) =& q^0_{31}(t) = 2/5[-\exp(-t/T_{1s}) + \exp(-t/T_{1f})],\\
q^0_{33}(t) =& 1/5[\exp(-t/T_{1s}) + 4\exp(-t/T_{1f})],\\
q^1_{11}(t) =& 1/5[3/2(1 + J_2/(J_2^2 - \omega_Q^2)^{1/2})\exp(-R^1_1 t) + 2\exp(-t/T_{2s})\\
&+ 3/2(1 - J_2/(J_2^2 - \omega_Q^2)^{1/2})\exp(-R^1_3 t)]\\
q^1_{12}(t) =& q^1_{21}(t) = \mathrm{i}/2\sqrt{3/5}\omega_Q/(J_2^2 - \omega_Q^2)^{1/2}[\exp(-R^1_1 t) - \exp(-R^1_3 t)]\\
q^1_{13}(t) =& q^1_{31}(t) = \sqrt{6}/5[1/2(1 + J_2/(J_2^2 - \omega_Q^2)^{1/2})\exp(-R^1_1 t) - \exp(-t/T_{2s})\\
&+ 1/2(1 - J_2/(J_2^2 - \omega_Q^2)^{1/2})\exp(-R^1_3 t)]\\
q^1_{22}(t) =& 1/2[(1 - J_2/(J_2^2 - \omega_Q^2)^{1/2})\exp(-R^1_1 t)\\
&+ (1 + J_2/(J_2^2 - \omega_Q^2)^{1/2})\exp(-R^1_3 t)]\\
q^1_{23}(t) =& q^1_{32}(t) = \mathrm{i}/\sqrt{10}\omega_Q/(J_2^2 - \omega_Q^2)^{1/2}[\exp(-R^1_1 t) - \exp(-R^1_3 t)]\\
q^1_{33}(t) =& 1/5[(1 + J_2/(J_2^2 - \omega_Q^2)^{1/2})\exp(-R^1_1 t) + 3\exp(-t/T_{2s})\\
&+ (1 - J_2/(J_2^2 - \omega_Q^2)^{1/2})\exp(-R^1_3 t)]\\
q^2_{22}(t) =& 1/2[(1 + J_1/(J_1^2 - \omega_Q^2)^{1/2})\exp(-R^2_1 t)\\
&+ (1 - J_1/(J_1^2 - \omega_Q^2)^{1/2})\exp(-R^2_2 t)]\\
q^2_{23}(t) =& q^2_{32}(t) = -\mathrm{i}/2\omega_Q/(J_1^2 - \omega_Q^2)^{1/2}[\exp(-R^2_1 t) - \exp(-R^2_2 t)]\\
q^2_{33}(t) =& 1/2[(1 - J_1/(J_1^2 - \omega_Q^2)^{1/2})\exp(-R^2_1 t)\\
&+ (1 + J_1/(J_1^2 - \omega_Q^2)^{1/2})\exp(-R^2_2 t)]\\
q^3_{33}(t) =& \exp(-t/T_{2s}),
\end{aligned}
\tag{A.6}
$$

whereas the relaxation rates and relaxation times are given by [19]

$$
\begin{aligned}
R^1_1 =& J_0 + J_1 + J_2 - (J_2^2 - \omega_Q^2)^{1/2}\\
R^1_3 =& J_0 + J_1 + J_2 + (J_2^2 - \omega_Q^2)^{1/2}\\
R^2_1 =& J_0 + J_1 + J_2 + (J_1^2 - \omega_Q^2)^{1/2}\\
R^2_1 =& J_0 + J_1 + J_2 - (J_1^2 - \omega_Q^2)^{1/2}\\
T_{1f} =& 1/(2J_1),\\
T_{1s} =& 1/(2J_2),\\
T_{2f} =& 1/Re(R^1_1),\\
T_{2s} =& 1/(J_1 + J_2).
\end{aligned}
\tag{A.7}
$$

Here J_0, J_1, and J_2 are the real part of the spectral density function at zero frequency, the Larmor frequency and two times the Larmor frequency, respectively.

A.3. Larmor precession

Larmor precession by an angle φ is implemented as a change of base by an angle $-\varphi$ [18]

$$
\begin{aligned}
\hat{T}_{lm}(s) &\to \cos(-m\varphi)\hat{T}_{lm}(s) + \sin(-m\varphi)\hat{T}_{lm}(a)\\
\hat{T}_{lm}(a) &\to \cos(-m\varphi)\hat{T}_{lm}(a) + \sin(-m\varphi)\hat{T}_{lm}(s).
\end{aligned}
\tag{A.8}
$$

Appendix B. Coefficients $\tilde{a}_{lm}$

After a preparation in the steady state, it must be assumed that all coherences are non-zero. σ is therefore written in its general form (Eq. (6)), and the observable signal after the coherence transfer pulse is computed using the expressions

Table B.1
Coefficients $\tilde{a}_{lm}$ as used in Section 2

m	l		
	1	2	3
0	-1	0	$\frac{\sqrt{6}}{4}$
1	$\frac{1}{2}$	$-\frac{1}{2}$	$-\frac{1}{8}$
2	0	$\frac{1}{2}$	$-\frac{\sqrt{10}}{8}$
3	0	0	$\frac{\sqrt{15}}{8}$

Coefficients $\tilde{a}_{lm}$ as introduced in Section 2 and in Eq. (B.3).

$$\sigma_{ss} \to \mathbf{R}(\omega_Q, t)\cdot[\mathbf{P}(\pi/2, \phi)\cdot\sigma_{ss} - \sigma_0] + \sigma_0, \tag{B.1}$$

$$S(t, \phi) \propto [\hat{T}_{11}(a) + \hat{T}_{11}(s)](t, \phi). \tag{B.2}$$

Arranging the terms according to $\exp(\mathrm{i}m\phi)$ it can be seen that $S(t, \phi)$ has the structure as shown in Eqs. (15)–(18). Straightforward calculation shows that

$$a_{l,-m}(t) = \tilde{a}_{lm}q^1_{1l}(t) = (-a_{l,m}(t))^*, \tag{B.3}$$

$$\tilde{a}_{l,-m} = -\tilde{a}_{l,m}. \tag{B.4}$$

The coefficients $\tilde{a}_{l,m}$ are summarized in Table B.1.

References

[1] H.Y. Carr, Phys. Rev. 112 (5) (1958) 1693.
[2] M.L. Gyngell, J. Magn. Reson. 81 (1989) 474.
[3] A. Oppelt, R. Graumann, H. Barfuß, H. Fischer, W. Hartl, W. Schajor, Electromedica 54 (1) (1986) 15.
[4] O. Speck, K. Scheffler, J. Hennig, Magn. Reson. Med. 48 (2002) 633.
[5] R.J. Kim, J.A.C. Lima, E.-L. Chen, S.B. Reeder, F.J. Klocke, E.A. Zerhouni, R.M. Judd, Circulation 95 (1997) 1877.
[6] R.J. Kim, R.M. Judd, E.-L. Chen, D.S. Fieno, T.B. Parrish, J.A.C. Lima, Circulation 100 (2) (1999) 185.
[7] M. Horn, C. Weidensteiner, H. Scheffer, M. Meininger, M. de Groot, H. Remkes, C. Dienesch, K. Przyklenk, M. von Kienlin, S. Neubauer, Magn. Reson. Med. 45 (2001) 756.
[8] T. Neuberger, A. Greiser, M. Nahrendorf, P.M. Jakob, C. Faber, A.G. Webb, MAGMA 17 (3–6) (2004) 196–200.
[9] U. Eliav, H. Shinar, G. Navon, J. Magn. Reson. 98 (1992) 223.
[10] N. Bansal, V. Seshan, J. Magn. Reson. Imag. 5 (1995) 761.
[11] I. Hancu, F.E. Boada, G.X. Shen, Magn. Reson. Med. 42 (1999) 1146.
[12] M. Levij, J. de Bleijser, J.C. Leyte, Chem. Phys. Lett. 83 (1981) 1983.
[13] W.S. Hinshaw, J. Appl. Phys. 47 (1976) 3709.
[14] J.R.C. van der Maarel, J. Chem. Phys. 94 (7) (1991) 4765.
[15] T.B. Parrish, D.S. Fieno, S.W. Fitzgerald, R.M. Judd, Magn. Reson. Med. 38 (1997) 653.
[16] G.J. Bowden, W.D. Hutchison, J. Khachan, J. Magn. Reson. 67 (1986) 415.
[17] J.R.C. van der Maarel, Chem. Phys. Lett. 155 (3) (1989) 288.
[18] I. Hancu, J.R.C. van der Maarel, F.E. Boada, J. Magn. Reson. 147 (2000) 179.
[19] J.R.C. van der Maarel, Concepts Magn. Reson. A 19 (2) (2003) 97–116.
[20] J.R.C. van der Maarel, R.H. Tromp, J.C. Leyte, C. Erkelens, J.G. Hollander, Chem. Phys. Lett. 169 (6) (1990) 585.
[21] D.E. Woessner, N. Bansal, J. Magn. Reson. 133 (1998) 21.
[22] G. Jaccard, S. Wimperis, G. Bodenhausen, J. Chem. Phys. 85 (11) (1986) 6282.
[23] J.M. Dizon, J.S. Tauskela, D. Wise, D. Burkhoff, P. Cannon, J. Katz, Magn. Reson. Med. 35 (1996) 336.
[24] J.G. Van Emous, C.J.A Van Echteld, Magn. Reson. Med. 40 (1998) 679.